A&A 533, A80 (2011)
DOI: 10.1051/0004-6361/201116846

Astronomy & Astrophysics

Herschel observations of the Herbig-Haro objects HH 52-54⋆

P. Bjerkeli[1], R. Liseau[1], B. Nisini[2], M. Tafalla[3], M. Benedettini[4], P. Bergman[1], O. Dionatos[5], T. Giannini[2], G. Herczeg[6], K. Justtanont[1], B. Larsson[7], C. M^{c}Coey[8], M. Olberg[1], and A. O. H Olofsson[1]

[1] Department of Earth and Space Sciences, Chalmers University of Technology, Onsala Space Observatory, 439 92 Onsala, Sweden
e-mail: per.bjerkeli@chalmers.se
[2] INAF – Osservatorio Astronomico di Roma, via di Frascati 33, 00040 Monte Porzio Catone, Italy
[3] Observatorio Astronómico Nacional (IGN), Calle Alfonso XII, 3. 28014, Madrid, Spain
[4] INAF – Osservatorio Astrofisico di Arcetri, Largo E. Fermi 5, 50125 Firenze, Italy
[5] Centre for Star and Planet Formation, Natural History Museum of Denmark, University of Copenhagen, Øster Voldgade 5−7, 1350 Copenhagen, Denmark
[6] Max Planck Institut for Extraterestrische Physik, Garching, Germany
[7] Department of Astronomy, Stockholm University, AlbaNova, 106 91 Stockholm, Sweden
[8] University of Waterloo, Department of Physics and Astronomy, Waterloo, Ontario, Canada

Received 8 March 2011 / Accepted 14 June 2011

ABSTRACT

Context. The emission from Herbig-Haro objects and supersonic molecular outflows is understood as cooling radiation behind shocks, which are initiated by a (proto-)stellar wind or jet. Within a given object, one often observes both dissociative (J-type) and non-dissociative (C-type) shocks, owing to the collective effects of internally varying shock velocities.
Aims. We aim at the observational estimation of the relative contribution to the cooling by CO and H_2O, as this provides decisive information for understanding the oxygen chemistry behind interstellar shock waves.
Methods. The high sensitivity of HIFI, in combination with its high spectral resolution capability, allowed us to trace the H_2O outflow wings at an unprecedented signal-to-noise ratio. From the observation of spectrally resolved H_2O and CO lines in the HH52-54 system, both from space and from the ground, we arrived at the spatial and velocity distribution of the molecular outflow gas. Solving the statistical equilibrium and non-LTE radiative transfer equations provides us with estimates of the physical parameters of this gas, including the cooling rate ratios of the species. The radiative transfer is based on an accelerated lambda iteration code, where we use the fact that variable shock strengths, distributed along the front, are naturally implied by a curved surface.
Results. Based on observations of CO and H_2O spectral lines, we conclude that the emission is confined to the HH54 region. The quantitative analysis of our observations favours a ratio of the CO-to-H_2O-cooling-rate $\gg$1. Formally, we derived the ratio $\Lambda(\mathrm{CO})/\Lambda(o\text{-}H_2O) = 10$, which is in good agreement with earlier determination of 7 based on ISO-LWS observations. From the best-fit model to the CO emission, we arrive at an H_2O abundance close to 1×10^{-5}. The line profiles exhibit two components, one that is triangular and another that is a superposed, additional feature. This additional feature is likely to find its origin in a region that is smaller than the beam where the *ortho*-water abundance is smaller than in the quiescent gas.
Conclusions. Comparison with recent shock models indicate that a planar shock cannot easily explain the observed line strengths and triangular line profiles. We conclude that the geometry can play an important role. Although abundances support a scenario where J-type shocks are present, higher cooling rate ratios are derived than predicted by these types of shocks.

Key words. stars: formation – stars: winds, outflows – Herbig-Haro objects – ISM: jets and outflows – ISM: molecules

1. Introduction

Outflows have often been discovered through observations of Herbig-Haro objects (see e.g. Herbig 1950, 1951; Haro 1952, 1953) that trace the gas at highest velocity. Liseau & Sandell (1986) showed that HH-objects and outflows are physically associated, implying that they likely have the same exciting source.

Water is one of the coolants that is most sensitive to different types of shock chemistry (e.g. Bergin et al. 1998). Depending on the ionisation fraction, magnetic field strength, and velocity of the shock, water abundances can be elevated to different levels (Hollenbach et al. 1989). In J-type shocks (Jump shocks), where the magnetosonic speed is lower than the propagation of the pressure increase, the involved energies generally dissociate H_2 and all molecules with lower binding energies. As such the water abundance is generally low in J-type shocks, although it may re-form in the post-shock cooling region once pre-shock densities are sufficiently high. In C-type shocks, however, the pre-shock gas is partially heated due to traversing magnetic waves from the post-shock gas, and molecules can survive the passage of the shock (Draine 1980), where both the magnetic field and the

⋆ *Herschel* is an ESA space observatory with science instruments provided by European-led Principal Investigator consortia and with important participation from NASA. Complementary observations were made with the following. *Odin* is a Swedish-led satellite project funded jointly by the Swedish National Space Board (SNSB), the Canadian Space Agency (CSA), the National Technology Agency of Finland (Tekes), and Centre National d'Étude Spatiale (CNES). The Swedish ESO Submillimetre Telescope (SEST) located at La Silla, Chile was funded by the Swedish Research Council (VR) and the European Southern Observatory. It was decommissioned in 2003. The Atacama Pathfinder EXperiment (APEX) is a collaboration between the Max-Planck-Institut für Radioastronomie, the European Southern Observatory and the Onsala Space Observatory.

Table 1. Molecular line observations carried out with *Odin*, SEST, APEX and *Herschel*.

Telescope	Molecule	Frequency (GHz)	E_u/k_B (K)	HPBW ($''$)	η_{mb}	Date (YYMMDD)	t_{int} (h)
SEST	CO (2–1)	230.538	16.6	23	0.50	970811-980806	3
SEST	CO (3–2)	345.796	33.2	15	0.25	970811-980806	3
APEX	CO (4–3)	461.041	55.3	14	0.60	070918	0.5
Odin	CO (5–4)	576.268	83.0	118	0.90	050502-050620	4
APEX	CO (7–6)	806.652	155.9	8	0.43	070918	0.8
Herschel-HIFI	CO (10–9)	1151.985	304.2	19	0.66	090726-100221	9
Odin	H_2O (1_{10}–1_{01})	556.936	42.4	126	0.90	090609-100420	12
Herschel-HIFI	H_2O (1_{10}–1_{01})	556.936	42.4	39	0.76	100729	0.05
Herschel-PACS	H_2O (2_{12}–1_{01})	1669.905	79.5	13	N/A	090226	0.1

gas density is compressed. In this type of shock, the activation barrier for neutral-neutral reactions between molecular hydrogen and oxygen is reached, and the water abundance is expected to become enhanced. This can be both the effect of sputtering from dust grains (Kaufman & Neufeld 1996) and high temperature chemistry occurring in the shocked region (Bergin et al. 1998). After the shock passage, the enhanced water abundance persists for a long time in the post-shock gas.

The atmosphere of the Earth is opaque at the wavelength of the lowest rotational transitions of water, as well as of most other higher excited transitions. Thus, it is not until recent years with the use of space-based observatories that these transitions have been observed successfully. Previous missions, such as SWAS (Melnick et al. 2000) and *Odin* (Nordh et al. 2003), have put constraints on the water abundance and the dynamics of molecular outflows (Franklin et al. 2008; Bjerkeli et al. 2009). None of these missions, however, have provided the spatial and spectral resolution that is available with the *Herschel* Space Observatory (Pilbratt et al. 2010).

HH 54 is a Herbig-Haro object located in the Chamaeleon II cloud at a distance of approximately 180 pc (Whittet et al. 1997). The visible objects in HH 54 are moving at high Doppler speed out of the cloud toward the observer, with velocities between $\sim$10 km s^{-1} and $\sim$10^2 km s^{-1} (Caratti o Garatti et al. 2009). The objects show a clumpy appearance due either to Rayleigh-Taylor instabilities in the flow or to variability in the jet itself. Another possibility is patchy overlying dust extinction. The source of the jet is not well constrained. This is discussed further in Appendix A.2, where we also present quantitative arguments for identifying IRAS 12553-7651 (ISO-Cha II 28) as the HH54 jet-driving source and its associated blueshifted CO outflow. No redshifted emission is observed as what would be expected from a bipolar jet (see Sect. 3). On the other hand, the extinction is relatively low, something that might allow the redshifted gas to flow out essentially unhindered into the low density material at the rear side of the cloud. It cannot, however, be ruled out that the outflow itself is one-sided and asymmetric. Recent simulations show that rapidly rotating stars with complex magnetic fields can be responsible for such flows (Lovelace et al. 2010).

HH 54 has previously been observed in various lines of CO, SiO, and H_2O using *Odin* and SEST (Bjerkeli et al. 2009; R. Liseau, unpublished). Several H_2O lines and high-J CO lines were also observed with ISO-LWS and published in Liseau et al. (1996) and Nisini et al. (1996). During the performance verification phase of the Heterodyne Instrument for the Far-Infrared (HIFI) instrument, aboard the *Herschel* Space Observatory, the CO (10–9) transition was observed. As part of the WISH keyprogram (van Dishoeck et al. 2011), the H_2O (1_{10}–1_{01}) and H_2O (2_{12}–1_{01}) transitions were also observed using HIFI and the Photodetector Array Camera and Spectrometer (PACS) respectively. We note that the wavelength region, covering the H_2O (2_{12}–1_{01}) transition, can also be observed with HIFI.

Table 2. Integrated intensities over the line wings and 1σ uncertainties in parentheses.

Line	Source	Δv_{LSR} (km s^{-1})	$\int T_{mb}\,dv$ (K km s^{-1})	$T_{mb,rms}$[a] (mK)
CO (2–1)	HH 54	0.9 to −23.3	34.6 (0.3)	224
CO (3–2)	HH 54	0.9 to −23.3	54.9 (1.9)	2021
CO (4–3)	HH 54	2.4 to −23.3	104.4 (3.9)	773
CO (5–4)	HH 54	2.4 to −21.8	9.3 (0.06)	20
CO (7–6)	HH 54	2.4 to −21.8	128.1 (25.3)	4741
CO (10–9)	HH 52	–	–	284
	HH 53	–	–	211
	HH 54	2.4 to −21.8	33.1 (0.3)	146
H_2O (1_{10}–1_{01})[b]	HH 54	2.4 to −22.8	9.2 (0.06)	20

Notes. [(a)] The velocity bin size when calculating the rms is the same as the channel spacing. [(b)] This refers to the spectra obtained with HIFI.

In this paper, we present observations, both from space and the ground, of HH 52–54 in spectral lines of CO and H_2O. We chose to observe this region based on the following three facts: HH54 is free of contamination from other objects, it is spatially confined, and it is resolved in the infrared regime with the instruments used. Using results from observations carried out with SEST, APEX, *Odin*, and *Herschel*, we aim at improving our understanding of interstellar shock waves. The observing modes and the instruments that have been used are described in Sect. 2, while the details of the HIFI data reduction can be found in Appendix B. The basic observational results are summarised in Sect. 3 and the interpretations discussed in Sect. 4.

2. Observations

The observations described in this paper were obtained between 1997 and 2010 with several different facilities. A summary of the observations is presented in Table 1 and the line intensities in Table 2.

2.1. Herschel

2.1.1. HIFI

During the performance verification phase of HIFI (de Graauw et al. 2010), the CO (10–9) data were obtained on 26–27 July 2009 and 21 February 2010. The H_2O data were obtained

29 July 2010. The 3.5 m Cassegrain telescope has a full width half maximum (*FWHM*) of 38″ at 557 GHz, 19″ at 1152 GHz, and 13″ at 1670 GHz. The HIFI $H_2O\,(1_{10}-1_{01})$ spectrum presented in this paper was obtained in point mode with position switch using band 1 (490–630 GHz). The OFF spectrum was obtained by a single observation of a reference point 10′ away. The CO (10–9) HIFI maps were obtained in two different observing modes using band 5 (1120–1250 GHz). In the dual-beam-switch raster mode, an internal chopper mirror is used to obtain an OFF spectrum 3′ away from the observed position. In the on-the-fly with position switch mode, the telescope is scanning the map area back and forth. The data were calibrated using the *Herschel Interactive Processing Environment* (HIPE) version 4.2 for the CO (10–9) and 5.0 for the $H_2O\,(1_{10}-1_{01})$ observations (Ott 2010). The data reduction of the HIFI maps is described in detail in Appendix B. For the CO (10–9) observation, data from one of the spectrometers on-board were used. The Wide Band Spectrometer (WBS) is an acousto-optical spectrometer with a 4 GHz frequency coverage. The channel spacing is 500 kHz (0.1 km s^{-1} at 1152 GHz and 0.3 km s^{-1} at 557 GHz). For the $H_2O\,(1_{10}-1_{01})$ observation, data from the High Resolution Spectrometer (HRS) have also been used. The HRS is an auto-correlator system (ACS) where the resolution can be varied from 0.125–1.00 MHz. For this observation it was set to 0.24 MHz. Observations from the horizontal (H) and the vertical (V) polarisations were combined for both observations. The spectra were converted to a $T_{\rm mb}$ scale using main beam efficiencies, $\eta_{\rm mb}$(1152GHz) = 0.66 and $\eta_{\rm mb}$(557 GHz) = 0.76 (Olberg 2010).

2.1.2. PACS

The PACS spectrograph (Poglitsch et al. 2010) is a 5 × 5 integral field unit array consisting of 9.″4 square spaxels (spatial picture elements). The observations were obtained on 26 February 2009 in line scan mode and cover the 178.8–180.5 μm region, centred on the $H_2O\,(2_{12}-1_{01})$ line at 179.5 μm. The blue channel simultaneously covered the 89.4–90.2 μm region, which is featureless and not discussed further. Two different nod positions, located 6′ from the target in opposite directions, were used to correct for the telescopic background. Data were reduced with HIPE version 4.0. The fluxes were normalised to the telescopic background and subsequently converted to an absolute flux based on PACS observations of Neptune (Lellouch et al. 2010), with an approximate uncertainty of ∼20% at 180 μm. The spatial resolution at 180 μm is nearly diffraction-limited (see Table 1). In well-centred observations of point sources, only about 40% of the light in the system falls within the central spaxel. The $H_2O\,(2_{12}-1_{01})$ line is spectrally unresolved in the R = 1700 spectra ($\Delta\upsilon \sim 175$ km s^{-1}).

2.2. Odin

The *Odin* space observatory carries a 1.1 m Gregorian telescope and was launched into space in 2001 (Nordh et al. 2003; Hjalmarson et al. 2003). It is located on a polar orbit at 600 km altitude. At 557 GHz, the *FWHM* is 126″ and at 576 GHz, 118″. The spectra were converted to a $T_{\rm mb}$ scale using a main beam efficiency, $\eta_{\rm mb}$ = 0.9, as measured from Jupiter observations (Hjalmarson et al. 2003).

The CO (5–4) observations suffered from frequency drift and were, for that reason, calibrated, using atmospheric spectral lines, acquired during the time intervals when *Odin* observed through the Earth's atmosphere (Olberg et al. 2003). Since the first publication of the CO (5–4) data in Bjerkeli et al. (2009), the frequency calibration scheme has improved. Despite this, the velocity scale for this particular observation has some uncertainties due to in-orbit variations of the local oscillator unit frequency. These variations are most likely caused by slight temperature changes in the spacecraft during each orbit, because the Earth is very close by. On a velocity scale these fluctuations correspond to a ∼2 km s^{-1} uncertainty.

A spectrum, showing a tentative detection of $H_2O\,(1_{10}-1_{01})$ at 557 GHz was published in Bjerkeli et al. (2009). Since then, however, additional observations toward HH 54 have been carried out in June 2009 and April 2010 for a total on-source time of 12 h.

The observing mode for both observations was position switching, where the entire telescope is re-orientated to obtain a reference spectrum (10′ away in June 2009 and 15′ away in April 2010). The spectrometer used is an acousto-optical spectrometer (AOS) where the channel spacing is 620 kHz (0.33 km s^{-1} and 0.32 km s^{-1} at 557 GHz and 576 GHz respectively). The data processing and calibration are described by Olberg et al. (2003).

2.3. SEST

The observations and calibration of the CO (2–1), CO (3–2), SiO (2–1), SiO (3–2) and SiO (5–4) data obtained with SEST have already been described in detail by Bjerkeli et al. (2009), to which we refer the interested reader.

2.4. APEX

CO (4–3) and CO (7–6) data were obtained with the APEX/FLASH receiver in service mode in July 2006. In this project[1], both CO lines were observed simultaneously on a grid map around HH54 B centred on α_{2000} = 12$^{\rm h}$55$^{\rm m}$49.$^{\rm s}$5, δ_{2000} = −76°56′23″. The selected reference position was relatively nearby at (120″, −120″), which resulted in contaminated line spectra close to the cloud LSR velocity (see below). The telescope pointing was checked by observing the nearby nova X Tra (IRAS 15094–6953). The map was spaced by half the instrument beam for the CO (4–3) transition, which corresponds to 7″ at 450 GHz. The data reduction was performed in CLASS, and the spectra were converted to a $T_{\rm mb}$ scale using the main beam efficiencies, 0.60 and 0.43 for the CO (4–3) and CO (7–6) transitions, respectively (Güsten et al. 2006). The channel spacing is 61 kHz (0.04 km s^{-1} at 461 GHz and 0.02 km s^{-1} at 807 GHz).

3. Results

The results from our observations are summarised in Table 2, where the integrated intensity over the blue line wing is presented.

3.1. Herschel

CO (10–9) is only detected in the HH 54 region. No emission is detected toward the region of HH 52-53 down to an rms level of ∼0.2 K (see upper panel of Fig. 1), and these objects are not discussed further. From the CO (10–9) emission, we estimate the size of the source to ∼27″. The $H_2O\,(1_{10}-1_{01})$ line

[1] ESO project code: 077.C-4005(A).

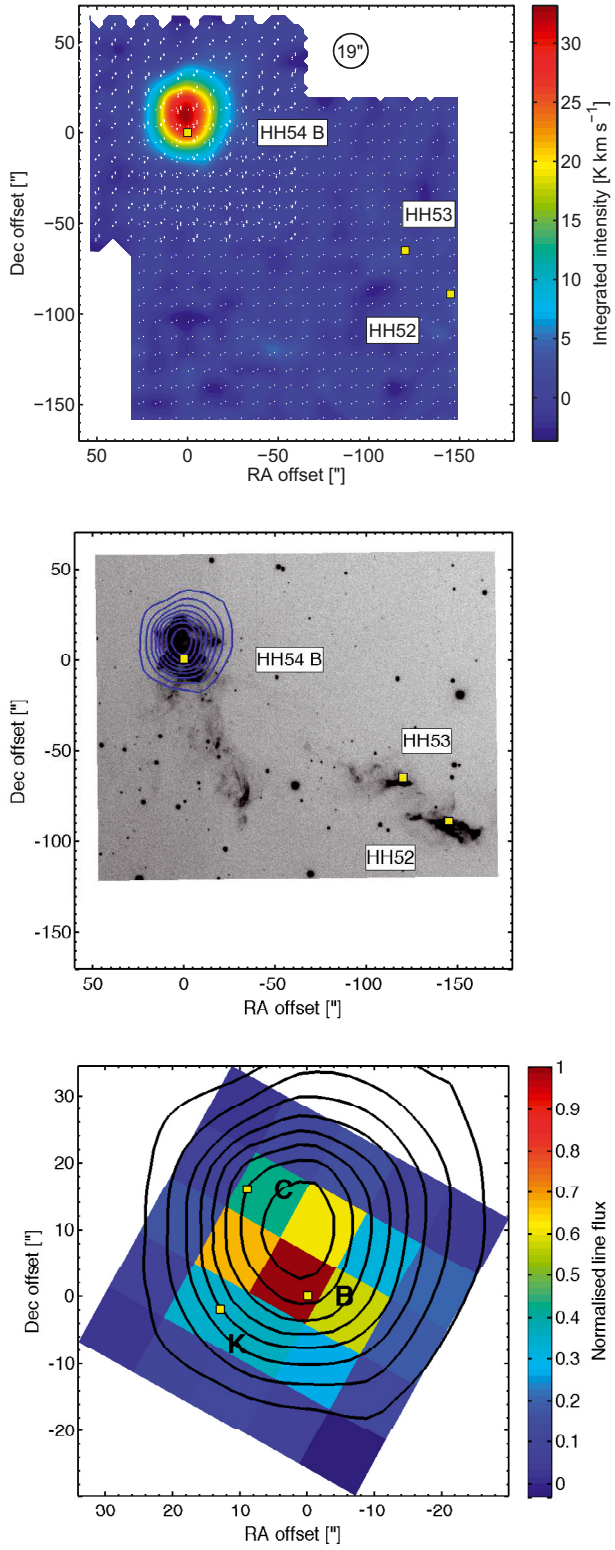

Fig. 1. *Upper panel*: false colour map of the CO (10–9) integrated intensity in the blue line wing (from +2.4 km s^{-1} to −30 km s^{-1}). The positions of HH 54 B, HH 53, and HH 52 are indicated with yellow squares. The readout positions for the on-the-fly and raster maps are indicated with white dots. *Middle panel*: CO (10–9) map of the integrated intensity obtained with HIFI in the blue line wing overlaid on an Hα image from Caratti o Garatti et al. (2009). Contours are from 5.5 to 33.6 K km s^{-1} in steps of 3.5 K km s^{-1}. *Lower panel*: a zoom of the CO (10–9) integrated intensity overlaid on the H_2O (2_{12}–1_{01}) emission obtained with PACS. The positions of HH 54 B, C and K as indicated in Giannini et al. (2006) are indicated with yellow squares.

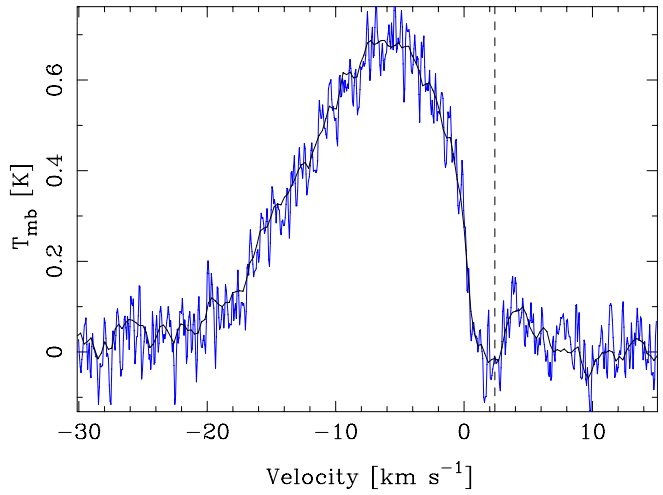

Fig. 2. H_2O (1_{10}–1_{01}) spectra obtained with HIFI. The blue spectral line is the HRS, and the black spectral line is the WBS. Both observations were centred on HH 54 B: $\alpha_{2000} = 12^h55^m50\overset{s}{.}3$, $\delta_{2000} = -76°56'23''$. The dashed line indicates the position of the velocity of the cloud.

is clearly detected toward HH 54 (see Fig. 2). Simultaneously, the NH_3(1_0–0_0) line at 572 GHz was covered in the upper side band. No emission is detected down to an rms level of ~20 mK. For the H_2O (2_{12}–1_{01}) line observed with PACS, emission is detected in most of the spaxels and the angular size of the source is no greater than ~28″. The peak flux in the central spaxel is 9 Jy. In the lower panel of Fig. 1, the CO (10–9) integrated intensity contours are shown overlaid on the H_2O (2_{12}–1_{01}) normalised flux in each spaxel. In this figure, each spaxel is presented on a square grid. In reality, however, there is a small misalignment between each spaxel (see Poglitsch et al. 2010, their Fig. 10). An offset of ~9″ between the CO (10–9) and the H_2O (2_{12}–1_{01}) emission peak is also observed, where the peak of the CO emission is located in between the B and C clumps as identified by Sandell et al. (1987). This offset might be real given a pointing accuracy of a few arcseconds for *Herschel*. Noteworthy is that the different clumps in the region show detectable proper motion on a time scale of a few years (e.g. Schwartz et al. 1984; Caratti o Garatti et al. 2006, 2009). However, the CO and H_2O observations with *Herschel* were obtained over a time span of only one year, and it is therefore unlikely that proper motion is the cause of the observed offset. The H_2O (1_{10}–1_{01}) spectra obtained with HIFI are presented in Fig. 2. The line is self absorbed by the foreground cloud at v_{LSR} = +2.4 km s^{-1}.

3.2. Odin

The *Odin* H_2O (1_{10}–1_{01}) observations carried out on 9 June 2009 and 20 April 2010 confirmed the previously published detection with an improved signal-to-noise ratio. It is this dataset that is used for the comparison with HIFI data in the present paper.

3.3. SEST

The CO (2–1) and CO (3–2) maps were centred with a slight offset with respect to HH 54 B, viz 4.″8. The spacing in CO (2–1) was 25″while the spacing between the observations in CO (3–2) were of the order 15″, i.e. one full beam width. The number of positions observed in the CO (2–1) map and the quality of the baselines in the CO (3–2) do not allow us to put constraints on the source size. SiO was not detected, when averaging all

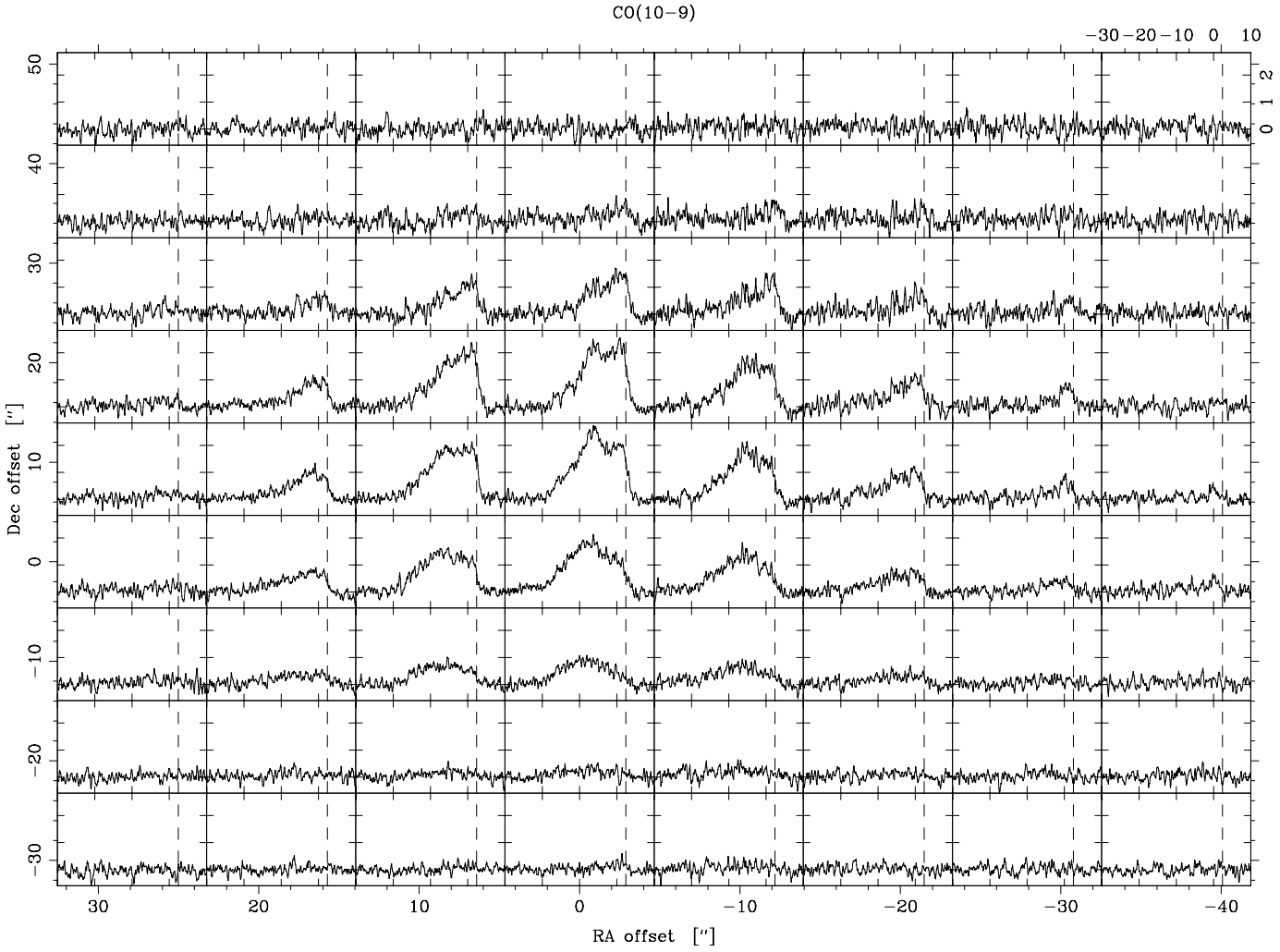

Fig. 3. CO (10−9) map obtained with HIFI. The map shows the spectra toward the region close to HH 54 B, and the map has been regridded with map spacing equal to 9.″3. Offsets are with respect to HH 54 B: $\alpha_{2000} = 12^{h}55^{m}50\overset{s}{.}3$, $\delta_{2000} = -76°56'23''$. The velocity scale ($\upsilon_{\rm LSR}$) and intensity scale ($T_{\rm mb}$) is indicated in the upper right corner of the map, $\upsilon_{\rm LSR} = +2.4$ km s^{-1} with a dashed line.

spectra together, down to an rms level of 10 mK for SiO (2−1), 15 mK for SiO (3−2), and 7 mK for SiO (5−4). The SEST data are presented in Fig. 4.

3.4. APEX

The quality of the FLASH data is not fully satisfactory, as they suffer from off-beam contamination near the line centre. However, as we here are mainly focussing on the line wings, this should affect our conclusions only a little, if at all. In these CO line maps, a bump feature (See Sect. 4.1) in the line profile was detected in some positions (at $\upsilon_{\rm LSR} = -7$ km s^{-1}, see below). A reliable source size from these maps can, however, not be determined. In both maps, the feature is detected in a velocity range spanning over $\Delta\upsilon \simeq 7$ km s^{-1} (see Fig. 4) .

Table 3. Parameters used in the CO model.

Parameters held constant	
Distance to source	$D_{\rm source} = 180$ pc
CO abundance	$X({\rm CO}) = 8 \times 10^{-5}$
LSR velocity	$\upsilon_{\rm LSR} = 2.4$ km s^{-1}
Velocity profile	$\upsilon(r) = 20\, r/R_{\rm max}$ km s^{-1}
Shell thickness	$\Delta r/R_{\rm max} = 0.12$
Source size	$\theta_{\rm source} = 30''$
Microturbulence	$\upsilon_{\rm turb} = 1.5$ km s^{-1}
Gas-to-dust mass ratio	$M_{\rm gas}/M_{\rm dust} = 100$
Emissivity parameter	$\kappa_{250\ \mu{\rm m}} = 25$ cm^2 g^{-1}
Dust frequency dependence	$\beta = 1$
Free parameters	
H_2 density	$n({\rm H_2}) = 1 \times 10^4$–$1 \times 10^8$ cm^{-3}
Kinetic temperature	$T_{\rm kin} = 10$–330 K

4. Discussion

4.1. Observed line profiles

Common to the observed transitions in CO and H_2O is that only blueshifted emission is detected. For all transitions, the maximum detected velocity in the line wing is of the order of −20 km s^{-1}. A bump-like feature at $\upsilon_{\rm LSR} \approx -7$ km s^{-1} is also clearly visible in the observed CO (10−9) and CO (2−1) spectra and possibly also in the CO (3−2), CO (5−4), and H_2O (1_{10}−1_{01}) data. In the CO (10−9) map, this feature is more prominent in some positions than others, and most likely it is spatially unresolved to *Herschel* (see Fig. 3). The $\upsilon_{\rm LSR} \simeq -7$ km s^{-1} component is also clearly visible in the CO (4−3) and

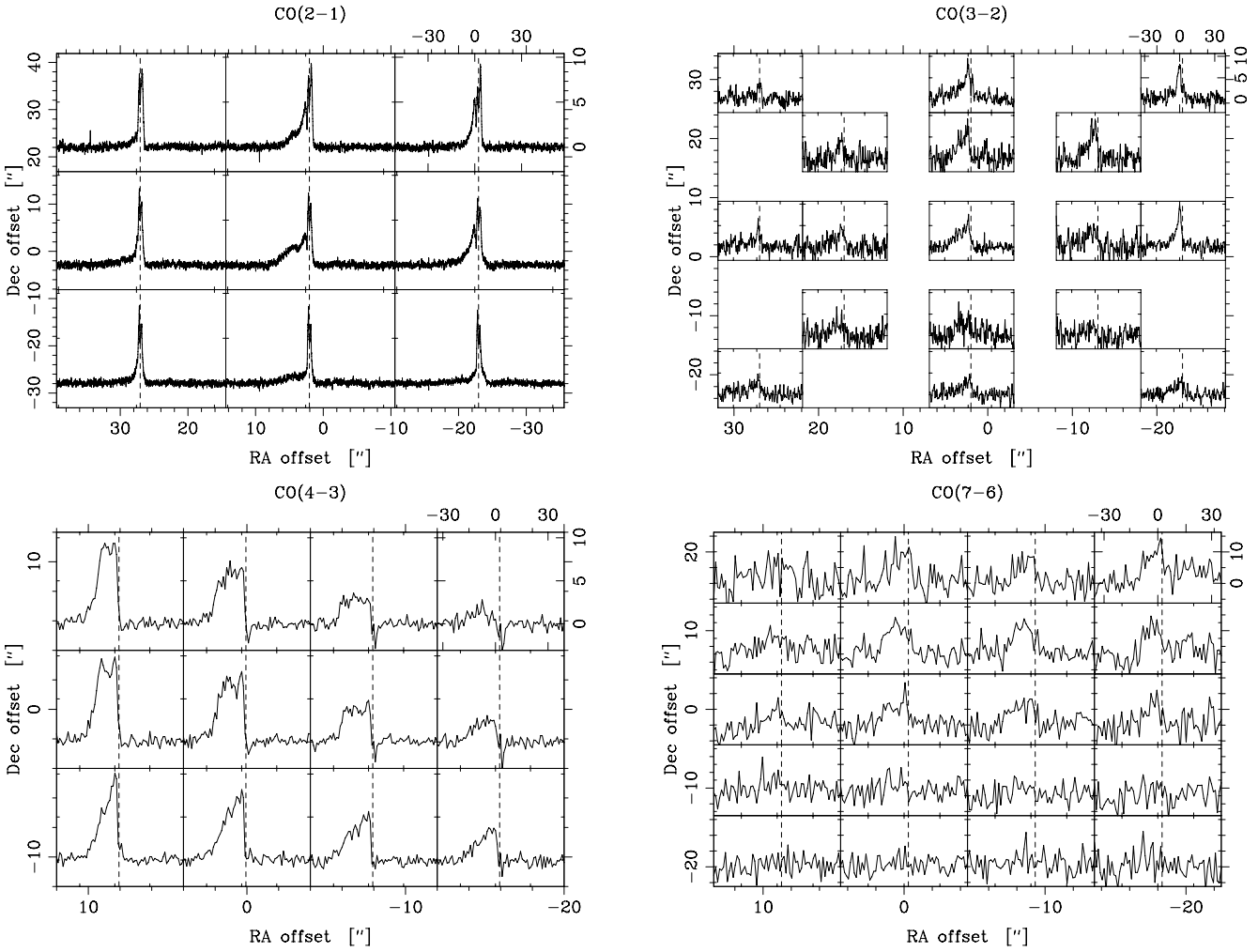

Fig. 4. Same as Fig. 3, but for the CO (2−1), CO (3−2), CO (4−3), and CO (7−6) maps obtained with SEST and APEX. The APEX maps have been regridded with a map spacing equal to 8″ for CO (4−3) and 9″ for CO (7−6). Note that the CO (4−3) spectra may be contaminated with OFF beam contribution.

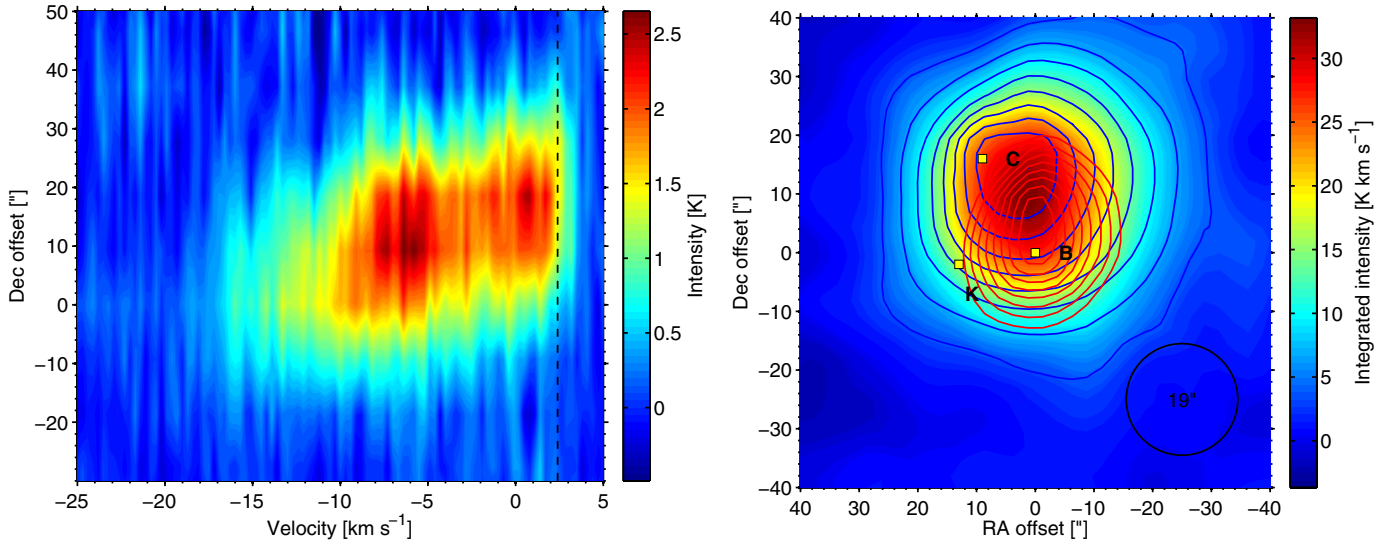

Fig. 5. *Left panel*: position (in Dec) velocity diagram of the HIFI CO (10−9) data showing the observed intensity. The bump-like feature can be seen at $v_{\rm LSR}$ = −7 km s^{-1}. The offset in RA is 0″. $v_{\rm LSR}$ =+2.4 km s^{-1} is indicated with a dashed line. *Right panel*: blue contours show the integrated intensity when the bump-like feature is subtracted from the spectra. Contours are from 3.6 to 28.7 K km s^{-1} in steps of 3.1 K km s^{-1}. Red contours show the integrated intensity for the bump. Contours are from 2.6 to 7.5 K km s^{-1} in steps of 0.6 K km s^{-1}. Underlying colours show the total integrated intensity over the observed line. The positions of HH 54 B, C and K are indicated with yellow squares.

CO (7−6) spectra observed with APEX (see Fig. 4) where the beam sizes are 13″ and 8″, respectively. Also in these maps, this component seems unresolved, so it likely originates in a region with an angular extent that is smaller than the telescope beams. In the CO (5−4) data, where the beam size is 118″, the bump-like feature is barely visible. This is expected if the beam filling factor is small. A position-velocity diagram of the CO (10−9) transition shows a trend where higher velocities are detected at lower declination and closer to the position of HH 54 B (see Figs. 3 and 5), i.e. where the H_2O ($2_{12}-1_{01}$) emission peaks (see Fig. 1). This is also clear in the right panel of Fig. 5 where the integrated intensity of the bump is presented together with the integrated intensity for the underlying triangular profile. The intensity maximum of the bump seems offset by ∼10″ south from the peak of the bulk outflow emission. The uncertainty attributed to this offset due to the baseline subtraction is ∼5″. Assuming that the apex of the shock is located close to the HH54 B position, one would also expect the highest velocities in this region.

4.2. Interpretation of the emission line data

To compute the line profiles for the observed emission, we used an accelerated lambda iteration (ALI) code (see Appendix C). The ALI code we used is a non-LTE, one dimensional code, assuming spherical geometry where several subshells are used. The number of cells and angles used in the ray tracing can also be arbitrarily chosen. In this work, a curved slab is compared with a plane parallel slab to interpret the observed spectral lines.

The formation of the observed spectral lines occurs most likely in shocked gas. Using results from detailed models of C-shocks, Neufeld et al. (2006) presents estimates of the excitation conditions for HH 54. From the analysis of H_2-rotation diagrams, Neufeld et al. (2006) have determined the presence of two different temperature regimes at 400 K and at 10^3 K.

We used their analytical expressions for the column density,

$$N(\mathrm{H_2}) = 7.9\times10^{20}\left[\frac{n(\mathrm{H_2})}{10^5}\right]^{0.5}\left(\frac{T_{\rm gas}}{1000}\right)^{-0.555}\ \mathrm{cm^{-2}}, \quad (1)$$

and for the velocity gradient,

$$\frac{\mathrm{d}\upsilon}{\mathrm{d}z} = 1.6\times10^{4}\left[\frac{n(\mathrm{H_2})}{10^5}\right]^{0.5}\left(\frac{T_{\rm gas}}{1000}\right)^{1.30}\ \mathrm{km\ s^{-1}\ pc^{-1}}, \quad (2)$$

to compute the emission in the CO and H_2O lines. Here $n(H_2)$ is the pre-shock density and the other quantities have their usual meaning. Following Neufeld et al. (2006) we take the compression factor of 1.5, which was used by them for H_2, but we assume that holds for CO as well. In addition, they assume that the fractional beam filling of the two temperature components is given by the ratio of the column density derived from the rotation diagram and that given by Eq. (1).

For these two temperatures and for pre-shock densitites[2] of 10^4 cm^{-3} and 10^5 cm^{-3}, we compute the emission in CO and H_2O lines from Eqs. (1) and (2) in plane-parallel slab geometry, including the shapes of the lines. Other parameters (such as CO abundance, source size, microturbulence, etc.) are given in Table 3. For the H_2O abundance we assume $X(H_2O) = 1.0\times10^{-5}$, consistent with the upper limit of $<2\times10^{-5}$ determined by Neufeld et al. (2006).

The results are presented in Figs. 7 and 9. As seen in the latter figure, the computed line strength of the ground state line of o-H_2O for a temperature of 400 K and pre-shock density of 10^5 cm^{-3} is not far from what HIFI has observed. On the other hand, such parameters do not agree with the observed CO (10−9) line, the intensity of which is severely over-predicted. As expected, the low-J lines CO (2−1) and CO (3−2) are not very sensitive to the changes in temperature from 400 to 1000 K. In all cases the computed rectangular line shape is different from the observed profiles, which have a pronounced triangular shape.

[2] These were the pre-shock densities used by Neufeld et al. (2006) to compute the H_2 abundance.

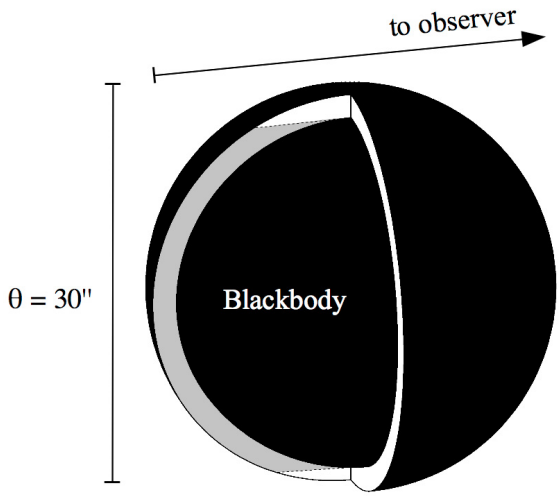

Fig. 6. A cut through the shells of the spherical model described in the text. Essentially all radiation originating from the rear side of the sphere (grey) is blocked out by the central blackbody source.

4.3. Emission originating in a curved slab

The spatial distribution of the gas also influences the observed line profiles (see e.g. Hartigan et al. 1987). For that reason we have also investigated a scenario in which the emission originates in a non-planar slab, which we refer to as curved slab in the following. To implement this we used a simple model that mimics an expanding shell with a diameter of 30″ located at a distance of 180 pc (see Fig. 6). The interior of the spherical shell is empty, i.e. at the temperature of cosmic background radiation field. This cold sphere occupies 88% of the radius of the sphere, based on a shell thickness of 5×10^{15} cm. This value lies between the slab thickness estimated by Liseau et al. (1996) and the analytical expression for the slab thickness at 180 K. The shell thickness is also consistent with the cooling length estimated by Kaufman & Neufeld (1996). Using this method, we block out essentially all the radiation originating in the opposite side of the sphere.

To compare with the observed line profiles, spectra were computed viewing the curved surface from the front. This is supported by the absence of detectable SiO emission which is often observed in molecular outflows with relatively high velocities (see e.g. Nisini et al. 2007). Shock modelling carried out by Gusdorf et al. (2008) suggests that sputtering is not very efficient in the velocity regime below 25 km s^{-1}. Therefore, if assuming that the outflow in HH 54 is observed from the front and that it has a small inclination angle with respect to the line of sight, the maximum velocity of the molecular gas is likely lower than this.

Inspection of the CO and H_2O spectra show a maximum radial velocity of ∼20 km s^{-1}. This is also consistent with the modelling by Giannini et al. (2006) who suggests a C+J type

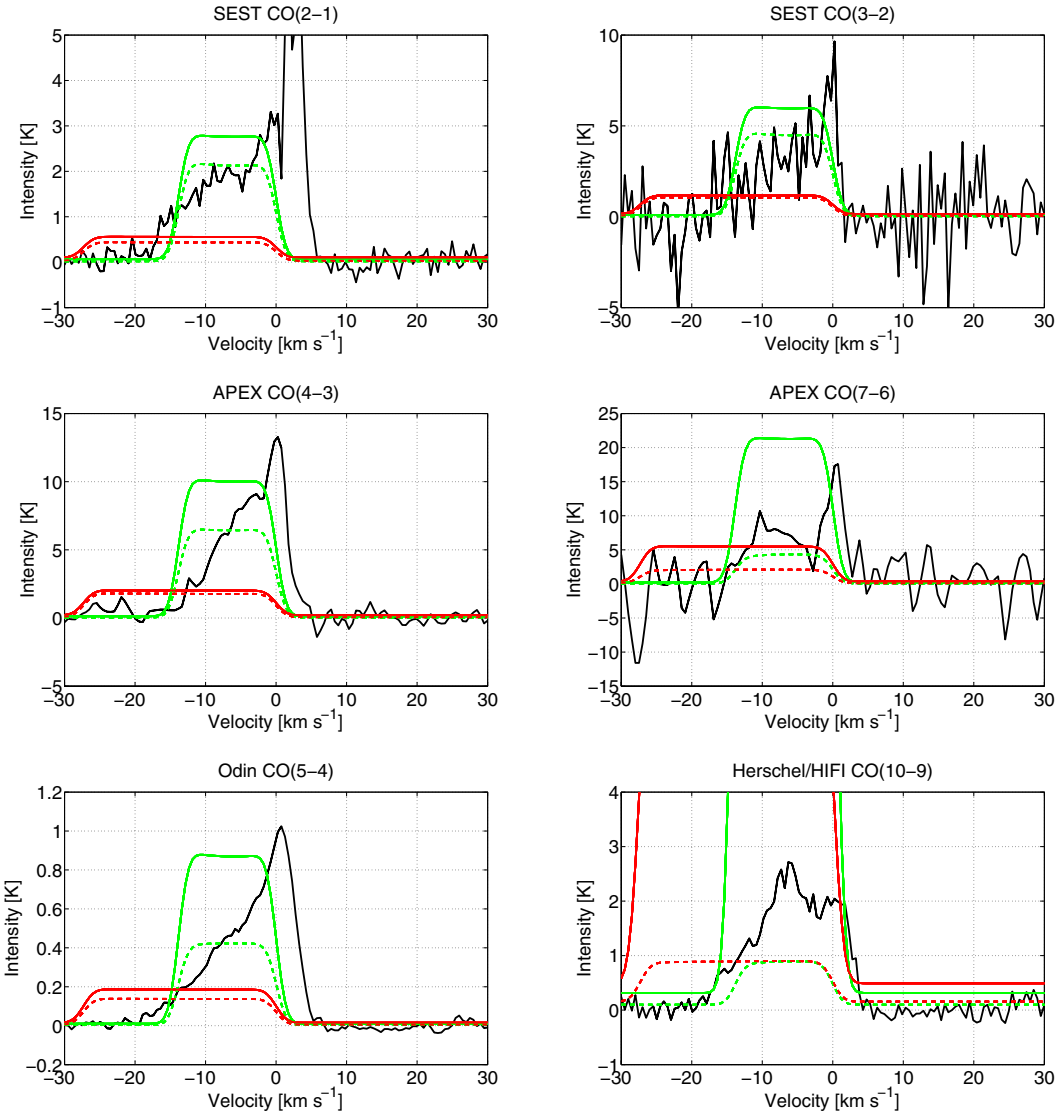

Fig. 7. The red (1000 K) and green (400 K) lines represent the model described in Neufeld et al. (2006), using pre-shock densities of 10^4 cm^{-3} (dashed) and 10^5 cm^{-3} (solid). The observed spectra from SEST, APEX, *Odin*, and HIFI are plotted with black solid lines. The modelled spectra have not been baselines subtracted.

shock with a maximum velocity of 18 km s^{-1}. The velocity in the shell increases linearly from 0 to 20 km s^{-1} (see Table 3). The true velocity profile is most likely more complicated. In a bow shock, the velocity component perpendicular to the jet direction is expected to be smaller than the component parallel to the jet direction. This makes the model somewhat simpler than reality. The velocity field within the shocked region probably also has a more complicated profile. Furthermore, we assume that the emission in all lines stem from the same region of size 30″. The bump-like feature discussed in Sect. 4.1, which indicates a deviation from a linear velocity profile, has not been considered in the modelling presented here. The parameters used in the model are summarised in Table 3.

We set up a grid where we vary the H_2 density from 10^4 to 10^8 cm^{-3} and the kinetic temperature of the gas from 30 to 330 K. Thus, our model is steady state and in equilibrium. We chose this approach in order to keep the number of free parameters as small as possible. Also, it is worth noting that we have not achieved a better fit to the bump-like feature (see Sect. 4.1) when varying the density and temperature profiles over the shells. To find the best-fit density and kinetic temperature, the reduced χ^2 is minimised, where the difference between the observed and the modelled intensity is evaluated in each velocity bin (see Fig. 10). The CO (2−1), CO (3−2), CO (5−4), and CO (10−9) lines are included in the χ^2-minimisation whereas the CO (4−3) and CO (7−6) lines are exluded due to the contamination from the off position and the high noise level of the CO (7−6) observation. For all the CO spectra, we only take the line wings into consideration, because emission from the surrounding cloud is clearly visible in the CO (2−1) spectra.

4.3.1. Density, temperature, and water abundance

From the curved slab model, the best-fit gas density and kinetic gas temperature are $n(H_2) = 9 \times 10^4$ cm^{-3} and $T_{\rm kin} = 180$ K (formally 177 K) respectively. This implies a total H_2 mass of $\sim 1 \times 10^{-2}\ M_\odot$. The value of the reduced χ^2 is 2.3. The CO spectra obtained with *Odin*, SEST and HIFI are plotted in Fig. 8, together with the modelled spectra. The model fits the observations well, and we conclude that the geometry of the region can be a crucial parameter determining the shape of the line profiles. The CO (10−9) line observed with *Herschel*, however, shows a

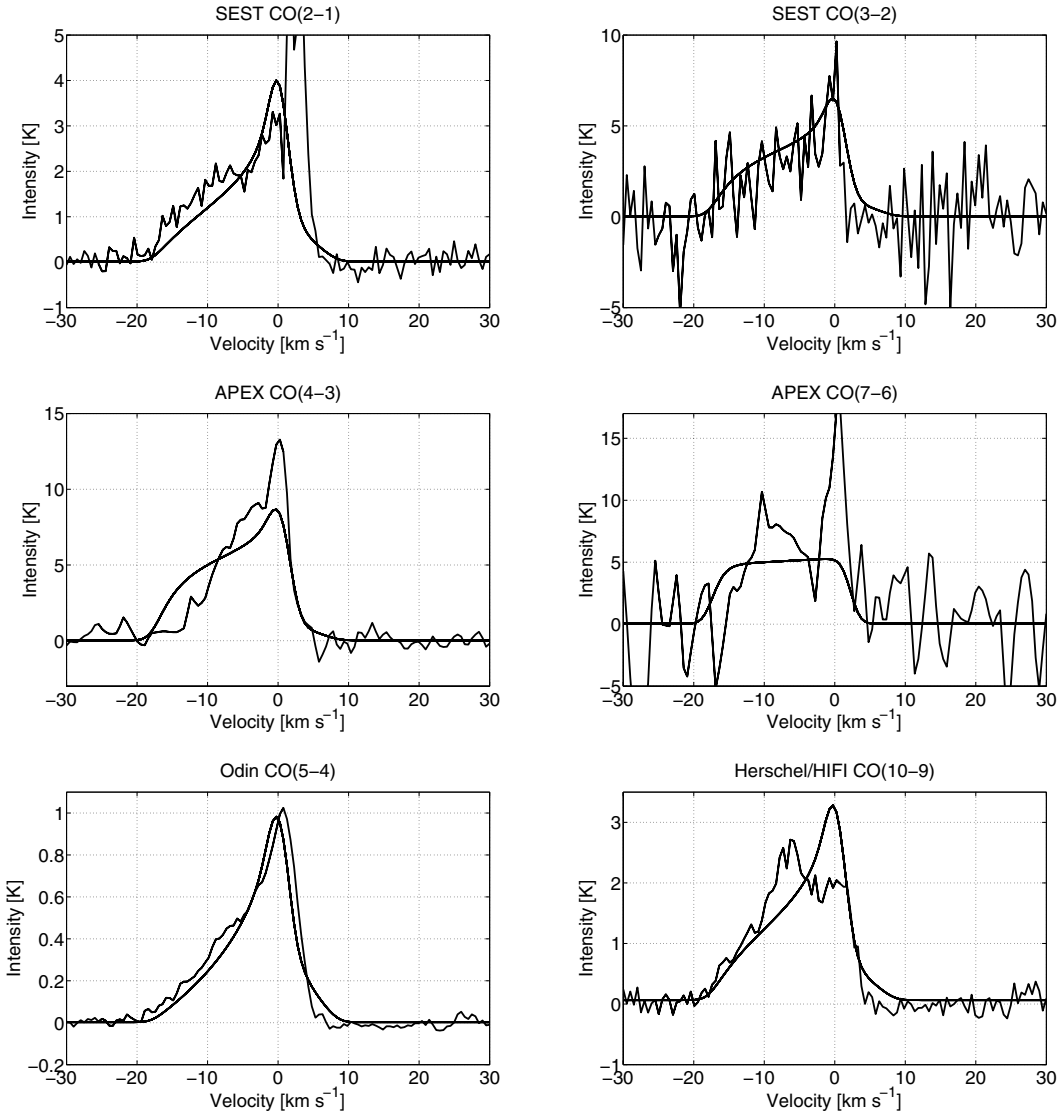

Fig. 8. The six spectra obtained with SEST, APEX, *Odin*, and *Herschel* compared to the best-fit model (see Sect. 4.3.1).

slightly more complicated profile than predicted (see discussion in Sect. 4.1). Thus, the triangular form is distorted by the presence of the $\upsilon_{\rm LSR} \simeq -7$ km s^{-1} feature. A minor change in the kinetic temperature (i.e. to 170 K) provides a better fit to the underlying triangular shape of the CO (10−9) line without affecting the lower-J CO lines by much. The computed maximum optical depths are $\leq 7 \times 10^{-2}$ for all the modelled CO lines. Using the gas density and kinetic temperature obtained from the CO modelling, the observed *o*-H_2O ground-state transition is best fit with an *ortho*-water abundance with respect to H_2 of $X(o\text{–}H_2O) = 1 \times 10^{-5}$ (see Fig. 11). The observed total flux in the map obtained with PACS corresponds to an integrated line intensity of 20 K km s^{-1}. This agrees with the integrated intensity from the predicted line profile to within a factor of 2.

4.3.2. H_2O line profile predictions

The line profiles for the six lowest rotational transitions of *ortho*-water have been computed. The abundance was set to 1×10^{-5} and the lines, which are predicted to be strong enough to be readily detected with HIFI, are displayed in Fig. 12. Also in this figure, redshifted emission originating in the opposite side of the sphere is present for the model with a curved slab. Significant changes in the excitation temperature in the inner and outer shells show up in these spectra as weak absorption features. For this reason, the spectra were computed using more than 100 shells to avoid any drastic changes in excitation temperature, due to optical depth effects between each shell. Simultaneously with the CO (10−9) observation, H_2O (3_{12}–2_{21}) at 1153 GHz was also observed. The observed noise level of ∼0.1 K is, however, too high to detect the line with a predicted strength of only ∼10 mK. A summary of these predictions is presented in Table 4. In this table, the observed integrated intensity in the H_2O (1_{10}–1_{01}) line is 30% lower than the predicted value due to the absorption from foreground gas. If this gas is at a low temperature, however, the higher transitions should not be affected much.

4.3.3. Cooling rate ratios

For the curved model described in Sect. 4.3, we derived the cooling ratio $\Lambda(\text{CO})/\Lambda(o\text{-}H_2O) = 10$ where the 557 GHz line is the

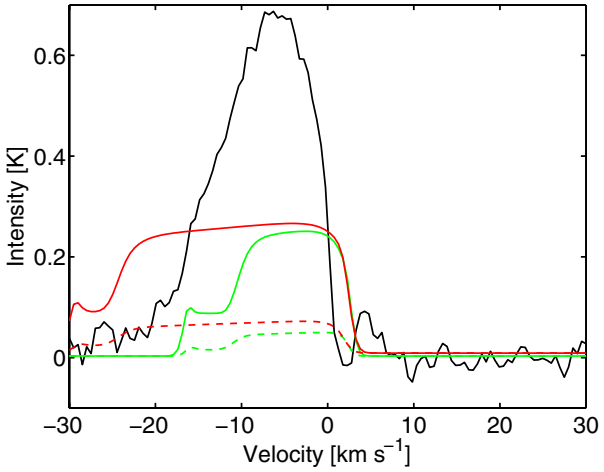

Fig. 9. The red (1000 K) and green (400 K) lines represent the model described in Neufeld et al. (2006), using pre-shock densities of 10^4 cm^{-3} (dashed) and 10^5 cm^{-3} (solid). The observed spectrum for the $H_2O\,(1_{10}-1_{01})$ transition with HIFI is plotted with a black solid line. The o-H_2O abundance is set to $X(o\text{–}H_2O) = 1\times10^{-5}$.

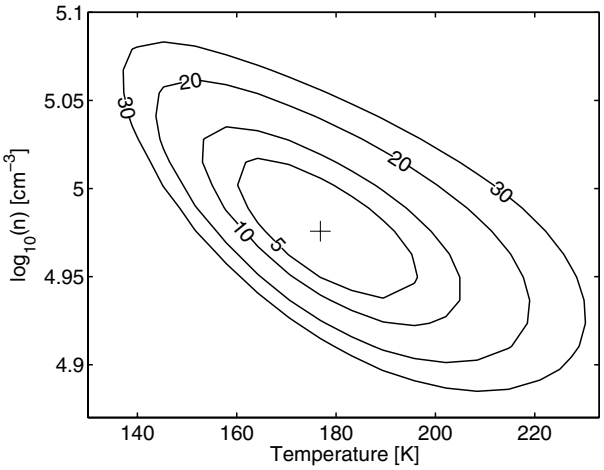

Fig. 10. Contour plot showing the sum of the chi-squares when comparing the modelled spectra and the observations. The 5%, 10%, 20%, and 30% deviations from the minimum value are indicated with solid lines. The best-fit density and temperature are indicated with a cross.

dominant contributor to the water cooling. This value agrees well with the earlier determined value of 7 based on ISO-LWS data and presented by Liseau et al. (1996).

4.3.4. The bump-like feature

As already discussed in Sect. 4.1, the bump-like feature seems unresolved to *Herschel*; i.e., the size of the source is uncertain. A source size comparable to the beam size of *Herschel*, at 1152 GHz (19″), would have to have a high temperature (>1000 K) and low density (~10^3 cm^{-3}) to fit the observations. This implies that the flux in the high-J CO lines would be higher than what was observed with ISO-LWS (Giannini et al. 2006). However, a source size as small as ~1″, where the temperature and density would have to be ~400 K and ~10^8 cm^{-3} respectively, is a plausible scenario. In that case however, the *ortho*-water abundance has to be less than 10^{-8} to fit with the ISO-LWS observations. In addition, the source is likely not smaller than 1″. Also in this case, the high-J CO lines would be stronger than what is actually observed.

Using a source size of 10″ (estimated size from H_2 maps presented in Neufeld et al. (2006)), the observed CO "bullet"-emission is well fit with a temperature of $T_{\rm kin}$ = 600 K and a density $n(H_2) = 2\times10^4$ cm^{-3}. This yields a column density $N(H_2) = 5\times10^{20}$ cm^{-2}. For an *ortho*-water abundance of $X(o\text{–}H_2O) = 1\times10^{-5}$, the $H_2O\,(3_{03}-2_{12})$ emission is entirely accounted for by the ISO-LWS observations. In this case the $H_2O\,(2_{12}-1_{01})$ emission would be merely about 25% of what was observed with PACS, and no significant contribution would be observed in the $H_2O\,(1_{10}-1_{01})$ line. Therefore, we conclude that the o-H_2O abundance in the "bullet" is likely lower than 10^{-5}.

4.3.5. Comparison with other results

The derived H_2 density implies a column density of 5×10^{20} cm^{-2}, which is approximately one order of magnitude higher than what is derived for the warm gas (Neufeld et al. 2006). The best-fit temperature, $T_{\rm kin}$ = 180 K, is significantly lower than the temperature in the gas responsible for the high-J CO emission [i.e. CO (14–13) – CO (20–19)] reported in

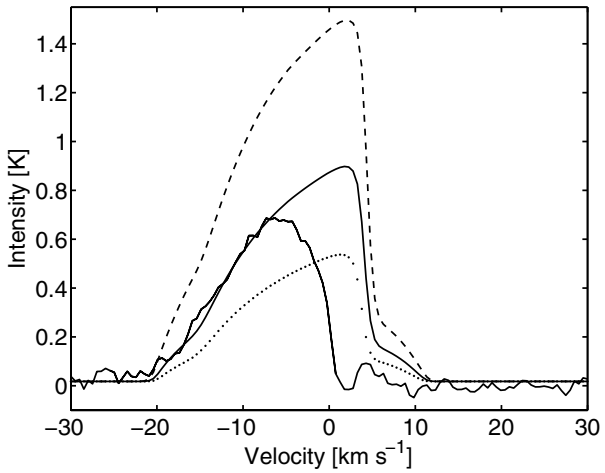

Fig. 11. The HIFI $H_2O\,(1_{10}-1_{01})$ spectrum compared with the model spectrum for $X(o\text{–}H_2O) = 1\times10^{-5}$. Spectra with the o-H_2O abundance increased by a factor of two (dashed line) and decreased by a factor of two (dotted line) are also included. Note that the foreground gas is visible in absorption in the observed spectrum.

Giannini et al. (2006). Our model predicts these lines to be one to two orders of magnitude weaker. Clearly, different temperature regimes are present in HH 54, and a one-temperature, one-density model cannot explain all the infrared observations. The high-J CO emission observed with ISO can be explained using the same geometry and source size but having a shell thickness 4×10^{14} cm, i.e. one order of magnitude thinner. In that case a slightly higher density ($n(H_2) = 1.5\times10^5$ cm^{-3}) and temperature (T = 500 K) fits the high-J CO lines well. On the other hand, this secondary component also makes a significant contribution to the CO (10–9) line, and this emission may originate in different regions. Recently, Takami et al. (2010) reported morphological differences between *Spitzer* observations in the 3.6, 4.5, 5.8, and 8.0 μm bands. The emission is observed to be less patchy in the long wavelength bands (i.e. 5.8 and 8.0 μm), and they interpret this as thermal H_2 emission being more enhanced in regions of lower density and temperature. Given that hot gas is obviously present in this region, the secondary component may

Table 4. The predicted integrated intensities, maximum intensities, continuum levels, and optical depths for the six lowest rotational transitions of *ortho*-water.

Line	ν (GHz)	*FWHM* ($''$)	Receiver	$\int T_{\rm mb} d\upsilon$ (K km s^{-1})	$10^{14} \int F_\lambda d\lambda$ (erg cm^{-2} s^{-1})	$T_{\rm mb,max}$ (K)	$T_{\rm cont}$ (mK)	$\tau_{\rm max}$
$1_{10}-1_{01}$	556.936	39	HIFI	12.9	9.3	0.88	18	40
$2_{12}-1_{01}$	1669.905	13	HIFI/PACS	13.0	28	0.80	80	44
$2_{21}-1_{10}$	2773.985	8	PACS	0.6	2.4	0.06	90	3.9
$2_{21}-2_{12}$	1661.017	13	HIFI/PACS	1.8	3.8	0.13	80	0.3
$3_{03}-2_{12}$	1716.775	13	HIFI/PACS	2.3	5.4	0.15	80	0.5
$3_{12}-2_{21}$	1153.117	19	HIFI	0.1	0.2	0.01	65	<0.1
$3_{12}-3_{03}$	1097.365	20	HIFI	1.0	1.4	0.10	62	<0.1
$3_{21}-2_{12}$	3977.047	5	PACS	0.3	1.3	0.02	103	0.3

Notes. The maximum and integrated intensities are for the baselines subtracted spectra. The foreground absorption, visible in the observed $H_2O\,(1_{10}-1_{01})$ spectrum, is not considered in this table.

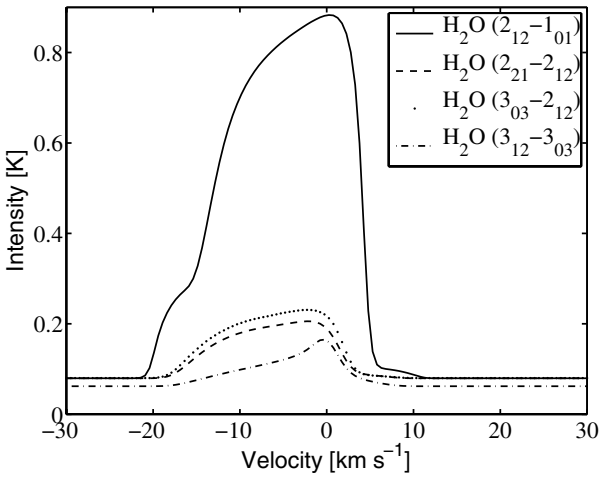

Fig. 12. Line profile predictions for the $H_2O\,(2_{12}-1_{01})$, $H_2O\,(2_{21}-2_{12})$, $H_2O\,(3_{03}-2_{12})$, and $H_2O\,(3_{12}-3_{03})$ spectra as observed with HIFI.

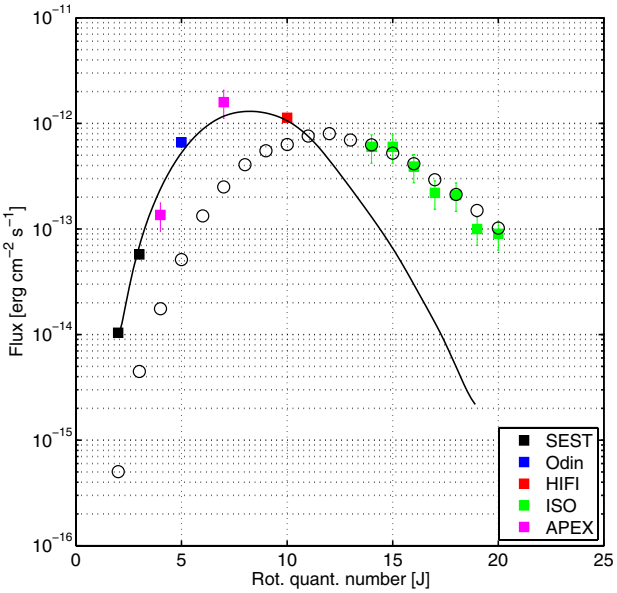

Fig. 13. Observed CO line fluxes (squares) as a function of the rotational quantum number J. The errorbars are the estimated calibration uncertainties (10% for SEST, *Odin*, and HIFI and 30% for APEX and ISO). The best-fit model, described in the present paper (see Sect. 4.3.1), is indicated with a solid line. The fit to the high-J CO lines is indicated with black circles (see Sect. 4.3.5).

in reality be in smaller regions of high temperature similar to those observed in H_2. In Fig. 13, the CO line flux is plotted as a function of the rotational quantum number, J.

The predicted integrated intensities can be compared with the modelling presented in Giannini et al. (2006). These authors present a multi-species analysis where they conclude that the observed H_2, CO, and H_2O lines can only be explained by a J-shock with magnetic precursor. The C+J shock model, presented in their paper, explains the observed $H_2O\,(2_{12}-1_{01})$ and $H_2O\,(3_{03}-2_{12})$ line fluxes of 7×10^{-13} erg cm^{-2} s^{-1} and 2×10^{-13} erg cm^{-2} s^{-1} well, and they predict that the line flux for the $H_2O\,(1_{10}-1_{01})$ line is 2.0×10^{-13} erg cm^{-2} s^{-1}. Converted to a K km s^{-1} scale, these values correspond to 6.8, 1.4, and 53 K km s^{-1} respectively. Taking the beam size into account, the predicted integrated intensity for the $H_2O\,(1_{10}-1_{01})$ line in this paper is at least a factor of four lower. This could be because this line is very sensitive to the type of shock present. This is also discussed in the paper by Giannini et al. (2006), where they note that a J type shock would change the flux by more than a factor of two downwards.

Recently, Flower & Pineau des Forêts (2010) presented theoretical predictions of CO and H_2O line intensities, based on detailed C- and J-type shock model calculations. Expectedly, the assumed magnetic fields are different for their models of C- and J-shocks, i.e. for $b = 1$ and $b = 0.1$, respectively, where b is defined through $B = b\sqrt{n_{\rm H}}\,\mu$G. For their high-density C-shocks (see below), this means that pre-shock fields of the order of $450\,\mu$G should be present. Based on OH Zeeman observations, Troland & Crutcher (2008) detected nine dark clouds in a sample of 34. Corresponding line-of-sight magnetic field strengths were in the range $B_{\rm los} = 10-25\,\mu$G, with typical values around $15\,\mu$G. As discussed by Troland & Crutcher (2008), for randomly oriented fields, $B_{\rm los} = 0.5\times|\boldsymbol{B}|$. Therefore, magnetic fields in dark clouds do not likely exceed levels of $20-50\,\mu$G. This refers to the observed scales of $3'$. However, these authors also show that in a given cloud $B_{\rm los}$ did not change appreciably from one position (active molecular outflow) to another (quiescent surrounding cloud). It seems, therefore, that fields as strong

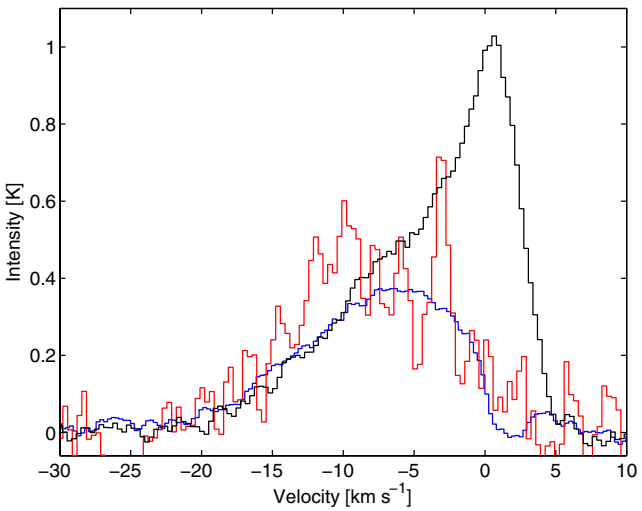

Fig. 14. Comparison between the CO (5–4) line (black) and the H_2O (1_{10}–1_{01}) line obtained with *Odin* (red). The H_2O spectrum has been multiplied by 6 for clarity. Also the HIFI H_2O (1_{10}–1_{01}) spectrum has been plotted in this figure for comparison (blue). The intensity of the emission has in this case been multiplied by 6 and corrected for beam filling.

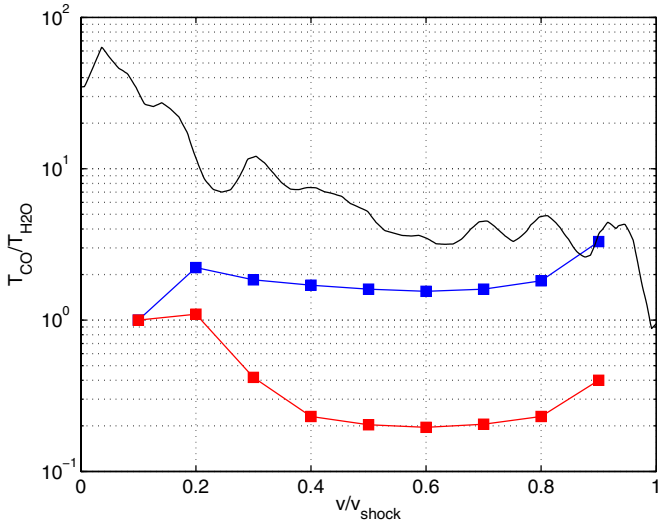

Fig. 15. Line ratios between CO (5–4) and H_2O (1_{10}–1_{01}). The ratio as measured from *Odin* is indicated with a black line. The predictions presented by Flower & Pineau des Forêts (2010) for υ_{shock} = 20 km s^{-1} are plotted in blue for n(H) = 2×10^4 cm^{-3} and in red for n(H) = 2×10^5 cm^{-3}.

as 450 μG may not be that common. On the other hand, order-of-magnitude lower field strengths (45 μG for b = 0.1) are more consistent with the observational evidence and may promote the occurrence of J-shocks.

For the radiative transfer, Flower & Pineau des Forêts (2010) used an LVG approximation in slab geometry. In their Fig. 8, line profiles for CO (5–4) and H_2O (1_{10}–1_{01}) are shown for C-shocks with two densities and four shock velocities. These lines are close in frequency and observations of HH 54 with Odin are made with essentially the same telescope beam, rendering resolution issues to be of only minor importance; i.e., any scaling of the intensities due to the source size should affect both observed lines in the same way. It should be feasible, therefore, to directly compare the line profiles of our Odin observations with those of the models by Flower & Pineau des Forêts (2010). Based on the observed maximum radial velocities, we consider only the models with $\upsilon_s \geq 20$ km s^{-1}. Their models with shock velocities of 20 km s^{-1} could correspond to a head-on view, whereas their models for υ_s = 30 and 40 km s^{-1} could correspond to inclinations of the flow with respect to the line of sight of 48° and 60°, respectively[3].

For the C-shock models, several of the line profiles display shapes that are qualitatively similar to those observed with *Odin* and HIFI. These line shapes are a consequence of the computed flow variables, not a geometry effect. However, in particular for the range of $\Delta\upsilon \sim 0$ to about 10 km s^{-1}, the *Odin*/HIFI lines exhibit CO-to-H_2O intensity ratios that are very much in excess of unity; i.e., $T_{CO}(\Delta\upsilon)/T_{H_2O}(\Delta\upsilon) \gg 1$. $\Delta\upsilon$ is the velocity relative to the rest frame of the flow, i.e. υ_{LSR}.

These observed ratios are much higher than the theoretical values (Figs. 14 and 15). Although the ratios are greater than unity for the low-density ($n_H = 2\times10^4$ cm^{-3}) C-shocks, these still fall far below the observed ones. On the other hand, the high-density ($n_H = 2\times10^5$ cm^{-3}) cases could be dismissed directly, because they tend to show *inverted* ratios, i.e. $T_{CO}/T_{H_2O} \ll 1$, contrary to what is observed (Fig. 15).

[3] For the emission knots of HH 54, Caratti o Garatti et al. (2006) determine an average inclination of 27°, which would imply that $\upsilon_s \sim \upsilon_{obs}$.

For the J-shock models, Flower & Pineau des Forêts (2010) list the predicted integrated intensities. Also in this case, the predicted CO-to-H_2O ratios (for a shock velocity of 20 km s^{-1}) are much lower than the observed ratio, viz. 0.06 and 0.005 for the pre-shock densities $n_H = 2\times10^4$ cm^{-3}and $n_H = 2\times10^5$ cm^{-3} respectively.

4.4. Implications for future work

The modelling of planar C-shocks shows that low densities are required for cooling rate ratios, Λ(CO)/Λ(o-H_2O) > 1, in contrast to our own findings, where densities at least as high as 10^5 cm^{-3} seemed implied by the observations (Sect. 4.3.1). The cause for this mismatch is not clear to us, but one of the reasons could be the difference between modelled planar and curved slab. Such modelling should therefore be attempted. The relatively high cooling rate ratio, Λ(CO)/Λ(o-H_2O) = 10, is also not easily reconciled with the presence of a C-type shock where a ratio, Λ(CO)/Λ(o-H_2O) $\ll$ 1 is favoured. On the other hand, J-shock models predict even smaller ratios than C-shock models. However, the relatively low *ortho*-water abundance determined from the modelling indicates that J-type shocks may contribute.

As already discussed in Sect. 4.3.5, different temperature regimes are present in the HH 54 region. It would be adequate therefore, to repeat the ISO-LWS observations, using the higher sensitivity and spatial resolution provided by PACS. The mid-J CO lines fall in the wavelength range covered by the Spectral and Photometric Imaging REceiver (SPIRE) and these should be observed.

5. Conclusions

Based on spectral mapping with *Herschel* of the region containing the Herbig-Haro Objects HH 52 to HH 54 we conclude the following:

- The CO (10–9) 1152 GHz line was clearly detected only toward the position of HH 54 with an *FWHM* $\lesssim 30''$, which is comparable to the extent of the HH-emission knots in the visible and infrared.

- The $H_2O\,(2_{12}-1_{01})$ 1669 GHz line was clearly detected toward HH 54, with a similar extent as the CO (10–9) line. An offset of 9″ (2.4×10^{16} cm) between the two species is observed, but the reality of this cannot be firmly assessed at present . The $H_2O\,(1_{10}-1_{01})$ 557 GHz line was also clearly detected toward HH 54.
- The CO (10–9) spectra show only blueshifted emission, with maximum relative velocities in excess of $-20\,\mathrm{km\,s^{-1}}$. The line profiles exhibit typically a triangular shape, which in certain positions is, however, contaminated by a bump-like feature at $\upsilon_{\rm LSR} = -7\,\mathrm{km\,s^{-1}}$. This feature is constant in velocity and width. It is limited in spatial extent and may be identified by what is commonly called a "bullet". Comparison of the observed spectra with analytical bow shock line profiles limits the viewing angle to greater than zero but $\lesssim 30°$.
- The bump is clearly seen in position-velocity cuts, revealing two peaks, in addition to a smooth velocity gradient of about $10^3\,\mathrm{km\,s^{-1}\,pc^{-1}}$. The low-velocity peak appears close to the ambient cloud velocity, whereas the second peak corresponds to the bump. For this feature we determine a relative peak-$T_{\rm mb} = 1.5$ K, $\upsilon_{\rm LSR} = -7\,\mathrm{km\,s^{-1}}$ and $FWHM = 5\,\mathrm{km\,s^{-1}}$ from Gaussian fit measurement of the CO (10–9) data.
- These line features are also observed in the CO (5–4) spectrum observed with Odin and in spectra obtained from the ground, i.e. in maps of the (2–1), (3–2), (4–3), and (7–6) CO transitions. In addition to the triangular line shape, these data therefore also confirm the reality of the spectral bump.
- We initially used physical parameters for shock models of HH 54 found in the literature to compute the CO spectra. These models presented two-component fits, given by analytical expressions for temperature and density in the respective slabs. These models were only moderately successful in reproducing the observational results, especially in the context of line shapes. Considerable improvement was found, however, in computed spectra using a curved slab instead.
- Using the best-fit model parameters (in a χ^2-sense) for the CO data we computed spectra for H_2O. This model fits the H_2O 557 GHz line observed with HIFI for an ortho-water abundance with respect to molecular hydrogen, $X(H_2O) = 1 \times 10^{-5}$.
- A cooling rate ratio, $\Lambda(\mathrm{CO})/\Lambda(o\text{-}H_2O) \gg 1$, is not easily reconcilable with recent shock modelling. On the other hand, a relatively low water abundance ($\sim 10^{-5}$) supports a scenario where J-shocks contribute significantly to the observed emission. This is also consistent with magnetic field strengths measurements toward dark clouds, where B-values that are lower than what is needed for C-type shocks are typically observed.
- Comparison of our *Odin* data with line profiles from recent detailed C-shock model computations in the literature suggests that some refinements of these models may be required.

Acknowledgements. The authors appreciate the support from A. Caratti o Garrati for providing the Hα image shown in Fig. 1. Aa. Sandqvist is thanked for scheduling the *Odin* observations of HH 54. We also thank the WISH internal referees Tim van Kempen and Claudio Codella for their efforts. HIFI has been designed and built by a consortium of institutes and university departments from across Europe, Canada and the United States under the leadership of SRON Netherlands Institute for Space Research, Groningen, The Netherlands and with major contributions from Germany, France and the US. Consortium members are: Canada: CSA, U. Waterloo; France: CESR, LAB, LERMA, IRAM; Germany: KOSMA, MPIfR, MPS; Ireland, NUI Maynooth; Italy: ASI, IFSI-INAF, Osservatorio Astrofisico di Arcetri – INAF; The Netherlands: SRON, TUD; Poland: CAMK, CBK; Spain: Observatorio Astronomico Nacional (IGN), Centro de Astrobiologia (CSIC-INTA). Sweden: Chalmers University of Technology – MC2, RSS & GARD; Onsala Space Observatory; Swedish National Space Board, Stockholm University – Stockholm Observatory; Switzerland: ETH Zurich, FHNW; USA: Caltech, JPL, NHSC.

Appendix A:

A.1. Extinction by dust and dust parameters

At the position of HH 54, the molecular cloud is relatively tenuous as the dust extinction through the cloud merely amounts to $A_{\rm V} \sim 2$–3 mag (Gregorio-Hetem et al. 1989; Cambrésy 1999). With the relations of Eqs. (2) and (8) of Hayakawa et al. (2001), this results in a total H_2-column density of $N(H_2) = 2 \times 10^{21}\,\mathrm{cm^{-2}}$.

From [Fe II] line observations, Gredel (1994) determined the visual extinction toward the HH object as $A_{\rm V} = 1$–3 mag, which could suggest that the blueshifted HH 54 is located at the rear side of the cloud, a circumstance that potentially explains the apparent absence of redshifted emission[4]. However, an $R_{\rm V}$-value of $\gtrsim 5$, which is significantly higher than that used by Gredel (1994) and by others, needs to be invoked to describe the Cha II dust (see the discussion by Alcalá et al. 2008, and references therein). This reflects a predominantly "big-grain" contribution to the extinction (almost 2 mag larger $A_{\rm V}$ per unit E_{B-V}), and we consequently chose a shallower dust opacity dependence on the wavelength in the FIR and submm, identified by the parameter β in Table 3, i.e. $\beta = 1$ as opposed to $\beta = 2$ for the general ISM. For the normalisation wavelength used by Hildebrand (1983), i.e. $\lambda_0 = 250\,\mu$m, we adopt the grain opacity $\kappa_0 = 25\,\mathrm{cm^2\,g^{-1}}$ (Ossenkopf & Henning 1994). The corresponding mass absorption coefficient κ at long wavelengths is then readily found from $\kappa_\lambda = \kappa_0(\lambda_0/\lambda)^\beta$.

Combining our own results with those found in the literature yields an SED of a putative core at 10 K which, provides a strict upper limit to the luminosity. Any associated central point source would have a limiting luminosity of $L_{\rm bol} < 0.4\,L_\odot$. Assuming optically thin emission at long wavelengths and using standard techniques, the mass of the 10 K core/envelope is estimated at a mere $2\,M_\oplus$, excluding the possibility of a very young age of the hypothetical central source.

A.2. The exciting source

Several IRAS point sources are found in the surroundings of HH 54, and it is plausible to assume that one of these would be the exciting source of the HH object. Most often, the exciting source is a young ($\lesssim$ Myr) stellar object, situated at the geometrical centre of the bipolar outflow, and this also seems to be the case for the CO outflow associable with IRAS 12515–7641[5] near HH 52 and HH 53 (Knee 1992). For HH 54, the situation is different, however: Knee (1992) identified IRAS 12522–7640, which is positionally coincident with HH 54, as the driving source of a collimated blueshifted outflow. It seems, however, very unlikely that this IRAS source is (proto-)stellar in nature. It was detected essentially only, and barely, in the 60 μm-band, and it was shown that this IRAS flux is entirely attributable to [O I] 63 μm line emission (Liseau et al. 1996). More recent observations by *Spitzer* are in support of this conclusion, as these

[4] From H_2-line emission at various positions of the HH object, Giannini et al. (2006) derive the essentially constant value of $A_{\rm V} = 1$ mag.

[5] Alcalá et al. (2008) identify this source as a likely background K-giant.

were unable to reveal any point source at this position (Alcalá et al. 2008).

On the basis of proper motion measurements and morphology considerations, Caratti o Garatti et al. (2009) propose the Class I object IRAS 12500−7658 to be the exciting source of HH 54. The IRAS source is located 20′ south of HH 54, i.e. at the projected distance of 1 pc. It was not detected at 1200 μm by Young et al. (2005, see below). What regards HH 52 and HH 53, no satisfactory candidate was found by these authors. The possibility of different exciting sources was also considered by Nisini et al. (1996) and Alcalá et al. (2008), associating HH 52 and HH 53 with IRAS 12496−7650 (DK Cha), whereas Ybarra & Lada (2009) also identify this object with the exciting source of HH 54.

In APEX-LABOCA maps at 870 μm, no emission was detected toward HH 54 nor from the Cha II cloud itself ($S_{870\,\mu m} < 20$ mJy beam^{-1}: van Kempen 2008). However, *jet-like* extensions are seen to emanate from both DK Cha and IRAS 12553−7651 (ISO-Cha II 28), which are situated some 10′ to 20′ south/southeast of HH 54. Narrow, extended emission from these IRAS sources was also reported by Young et al. (2005), who used SEST-SIMBA to map the region at 1200 μm. The alignment with the HH objects is poor, however. Based on the observed spectral indices, this emission is dominated by optically thin radiation from dust. The dust features appear as tori or rings seen edge-on, but given their sizes (3×10^4 AU), they do not represent what commonly is called a (protostellar) "disc". Perhaps these dust features are leftovers from an earlier history, during which the IRAS sources were formed. A "conventional disc" of size ∼2 AU could very well hide inside, and any outflow would be orthogonal to these disc features.

Whereas the dust extension from DK Cha is not, whether direct or perpendicular, pointing anywhere near HH 52-54, the vector orthogonal to the linear feature of ISO-Cha II 28, at position angle 51°, is within 5° from the current direction toward HH 54. Taking the uncertainty of this estimate into account, this coincidence appears very compelling. If this source drives/has driven a jet, that would very well be aligned with HH 54. The projected distance is 16′ (0.8 pc), i.e. jet travel times would be of the order of $10^4\,(\upsilon/100\,\mathrm{km\,s^{-1}})^{-1}$ yr. With a total luminosity of $\sim 10\,L_\odot$ and a mass accretion rate of $\dot{M}_{\rm acc} = 6 \times 10^{-7}\,M_\odot\,\mathrm{yr}^{-1}$ (Alcalá et al. 2008), ISO-Cha II 28 would make an excellent candidate[6] for the exciting source of HH 54, whose (distance-corrected) stellar mass loss rate has been determined as $\dot{M}_{\rm loss} \leq 4 \times 10^{-7}\,M_\odot\,\mathrm{yr}^{-1}$ (Knee 1992), assuming a flow velocity of $\geq$100 km s^{-1}. A ratio of loss-to-accretion rate of $\leq 2/3$ would thus be indicated, which is a value that is in reasonable agreement with theoretical expectation for centrifugally driven MHD winds (Königl & Pudritz 2000; Shu et al. 2000; Contopoulos & Sauty 2001). To summarise, and as concluded by others before, the issue of the exciting source(s) of the HH objects 52, 53, 54 essentially remains unsettled.

Appendix B: HIFI data reduction

The CO (10−9) data published in this paper are public to the scientific community and can be downloaded from the *Herschel* Science Archive[7] (HSA). The two CO (10−9) observations were carried out in dual-beam-switch raster mode (observation id: 1342180798) and on-the-fly with position switch mode (observation id: 1342190901). The H_2O (1_{10}−1_{01}) observation was carried out in point mode with position switch. The data reduction and production of the HIFI maps followed the following steps

1. The raw data were imported to HIPE from the HSA.
2. All data were recalibrated using v4.2 of the HIFI pipeline for CO (10−9) and v5.0 for H_2O (1_{10}−1_{01}). There is a slight offset between the pointings for the horizontal and vertical polarisations. For that reason, separate readout positions were calculated for the two polarisations.
3. The level 2 data were exported to Class using the HiClass tool in HIPE.
4. A baseline was fitted to and subtracted from each individual spectrum. This step and the subsequent data reduction were carried out in xs[8].
5. From Fig. 1, it is clear that the readout positions for the two CO (10−9) maps are not on a regular grid in RA and Dec. Instead of averaging nearby spectra together, a Gaussian weighting procedure was used. The *FWHM* of the two-dimensional Gaussian used in the weighting was taken to be 9.3″. This size is larger than the average spacing between individual spectra but, on the other hand, small enough not to change the spatial resolution significantly.
6. In order to verify the quality of the CO (10−9) observations, spectra taken toward the same positions in the two different observing modes were compared, showing no significant differences (see Fig. B.1). Also the horizontal and vertical polarisation data were reduced individually for both CO (10−9) and H_2O (1_{10}−1_{01}) showing excellent agreement.

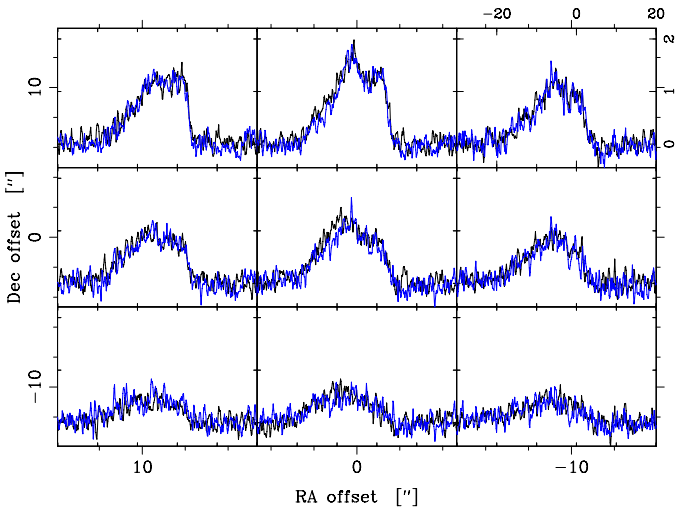

Fig. B.1. CO (10−9) spectra toward HH 54. The black spectra are from the HIFI observation 1342180798, while the blue spectra are from the observation 1342190901. The horizontal and vertical polarisations have been averaged together (see text).

Appendix C: Radiative transfer analysis

An ALI method (e.g. Rybicki & Hummer 1991) is used to compute the line profiles for the observed transitions, varying only

[6] From the data for CO outflows compiled by Wu et al. (2004) and complementing information in the literature, it is found that $L_{\rm bol} \propto \dot{M}_{\rm loss}^{\,x}$, where $x = 1.0$ for $\dot{M}_{\rm loss} < 10^{-5}\,M_\odot\,\mathrm{yr}^{-1}$ (for $\upsilon_{\rm wind} = 100$ km s^{-1}) and which steepens to $x = 1.2$ beyond that. This holds over eight orders of magnitude, albeit with considerable spread due to the inhomogeneity of the data. According to this relation, $L_{\rm bol} = 10\,L_\odot$ if $\dot{M}_{\rm loss} = 4 \times 10^{-7}\,M_\odot\,\mathrm{yr}^{-1}$.

[7] http://herschel.esac.esa.int/Science_Archive.shtml

[8] Data reduction software developed by P. Bergman at the Onsala Space Observatory, Sweden; http://www.chalmers.se/rss/oso-en/observations/

the density, kinetic temperature and the geometry of the shocked region. ALI is a method where the coupled problem of radiative transfer and statistical equilibrium is solved exactly.

C.1. Accelerated lambda iteration

The ALI code has in recent years been used in several publications (see e.g. Justtanont et al. 2005; Wirström et al. 2010) and was benchmarked with other codes in a paper by Maercker et al. (2008). The ALI technique is described in more detail in that paper. In the present work, typically 30 shells and 16 angles are used. The statistical equilibrium equations and the equation of radiative transfer are solved iteratively until the relative level populations between each iteration changes by less than 10^{-8}. In the modelling we set the energy limit to 2000 K and 27 rotational energy levels, 26 radiative transitions, and 351 collisional transitions are included in the calculations for CO. For *o*-H_2O, the corresponding numbers are 45, 164, and 990.

C.1.1. Collision rates

In recent years, substantial efforts have been made to determine cross-sections for H_2O excitation due to collisions with H_2. Quantal calculations governing collisions between H_2O and H_2 are to this date incomplete and for *o*-H_2O, only collision rates for interaction with *p*-H_2 are available (Dubernet et al. 2009). For this reason we make the assumption that all *p*-H_2 are in the lowest energy state when solving the statistical equilibrium equations. It is also assumed that the *p*-H_2 stays in the ground state after the collision. The ortho-to-para ratio has been estimated for warm H_2 by Neufeld et al. (2006). These authors derive ratios significantly lower than 3, viz. ∼0.4−2 in the HH 54 region. The computed spectra from the ALI modelling have also been compared with those, using the collision rates presented by Faure et al. (2007), and with similar results. In the case of CO, we use the collision rates presented by Yang et al. (2010).

References

Alcalá, J. M., Spezzi, L., Chapman, N., et al. 2008, ApJ, 676, 427
Bergin, E. A., Neufeld, D. A., & Melnick, G. J. 1998, ApJ, 499, 777
Bjerkeli, P., Liseau, R., Olberg, M., et al. 2009, A&A, 507, 1455
Cambrésy, L. 1999, A&A, 345, 965
Caratti o Garatti, A., Giannini, T., Nisini, B., & Lorenzetti, D. 2006, A&A, 449, 1077
Caratti o Garatti, A., Eislöffel, J., Froebrich, D., et al. 2009, A&A, 502, 579
Contopoulos, I., & Sauty, C. 2001, A&A, 365, 165
de Graauw, T., Helmich, F. P., Phillips, T. G., et al. 2010, A&A, 518, L6
Draine, B. T. 1980, ApJ, 241, 1021
Dubernet, M.-L., Daniel, F., Grosjean, A., & Lin, C. Y. 2009, A&A, 497, 911
Faure, A., Crimier, N., Ceccarelli, C., et al. 2007, A&A, 472, 1029
Flower, D. R., & Pineau des Forêts, G. 2010, MNRAS, 406, 1745
Franklin, J., Snell, R. L., Kaufman, M. J., et al. 2008, ApJ, 674, 1015
Giannini, T., McCoey, C., Nisini, B., et al. 2006, A&A, 459, 821
Gredel, R. 1994, A&A, 292, 580
Gregorio-Hetem, J. C., Sanzovo, G. C., & Lepine, J. R. D. 1989, A&AS, 79, 452
Gusdorf, A., Cabrit, S., Flower, D. R., & Pineau Des Forêts, G. 2008, A&A, 482, 809
Güsten, R., Nyman, L. Å., Schilke, P., et al. 2006, A&A, 454, L13
Haro, G. 1952, ApJ, 115, 572
Haro, G. 1953, ApJ, 117, 73
Hartigan, P., Raymond, J., & Hartmann, L. 1987, ApJ, 316, 323
Hayakawa, T., Cambrésy, L., Onishi, T., Mizuno, A., & Fukui, Y. 2001, PASJ, 53, 1109
Herbig, G. H. 1950, ApJ, 111, 11
Herbig, G. H. 1951, ApJ, 113, 697
Hildebrand, R. H. 1983, QJRAS, 24, 267
Hjalmarson, Å., Frisk, U., Olberg, M., et al. 2003, A&A, 402, L39
Hollenbach, D. J., Chernoff, D. F., & McKee, C. F. 1989, in Infrared Spectroscopy in Astronomy, ed. E. Böhm-Vitense, ESA SP, 290, 245
Justtanont, K., Bergman, P., Larsson, B., et al. 2005, A&A, 439, 627
Kaufman, M. J., & Neufeld, D. A. 1996, ApJ, 456, 611
Knee, L. B. G. 1992, A&A, 259, 283
Königl, A., & Pudritz, R. E. 2000, Protostars and Planets IV, 759
Lellouch, E., Hartogh, P., Feuchtgruber, H., et al. 2010, A&A, 518, L152
Liseau, R., & Sandell, G. 1986, ApJ, 304, 459
Liseau, R., Ceccarelli, C., Larsson, B., et al. 1996, A&A, 315, L181
Lovelace, R. V. E., Romanova, M. M., Ustyugova, G. V., & Koldoba, A. V. 2010, MNRAS, 408, 2083
Maercker, M., Schöier, F. L., Olofsson, H., Bergman, P., & Ramstedt, S. 2008, A&A, 479, 779
Melnick, G. J., Stauffer, J. R., Ashby, M. L. N., et al. 2000, ApJ, 539, L77
Neufeld, D. A., Melnick, G. J., Sonnentrucker, P., et al. 2006, ApJ, 649, 816
Nisini, B., Lorenzetti, D., Cohen, M., et al. 1996, A&A, 315, L321
Nisini, B., Codella, C., Giannini, T., et al. 2007, A&A, 462, 163
Nordh, H. L., von Schéele, F., Frisk, U., et al. 2003, A&A, 402, L21
Olberg, M. 2010, Technical Note: ICC/2010-nnn, v1.1, 2010-11-17
Olberg, M., Frisk, U., Lecacheux, A., et al. 2003, A&A, 402, L35
Ossenkopf, V., & Henning, T. 1994, A&A, 291, 943
Ott, S. 2010, in Astronomical Data Analysis Software and Systems XIX, ed. Y. Mizumoto, K.-I. Morita, & M. Ohishi, ASP Conf. Ser., 434, 139
Pilbratt, G. L., Riedinger, J. R., Passvogel, T., et al. 2010, A&A, 518, L1
Poglitsch, A., Waelkens, C., Geis, N., et al. 2010, A&A, 518, L2
Rybicki, G. B., & Hummer, D. G. 1991, A&A, 245, 171
Sandell, G., Zealey, W. J., Williams, P. M., Taylor, K. N. R., & Storey, J. V. 1987, A&A, 182, 237
Schwartz, R., Jones, B. F., & Sirk, M. 1984, AJ, 89, 1735
Shu, F. H., Najita, J. R., Shang, H., & Li, Z. 2000, Protostars and Planets IV, 789
Takami, M., Karr, J. L., Koh, H., Chen, H., & Lee, H. 2010, ApJ, 720, 155
Troland, T. H., & Crutcher, R. M. 2008, ApJ, 680, 457
van Dishoeck, E. F., Kristensen, L. E., Benz, A. O., et al. 2011, PASP, 123, 138
van Kempen, T. 2008, Ph.D. Thesis, Leiden Observatory, Leiden University, P.O. Box 9513, 2300 RA Leiden, The Netherlands
Whittet, D. C. B., Prusti, T., Franco, G. A. P., et al. 1997, A&A, 327, 1194
Wirström, E. S., Bergman, P., Black, J. H., et al. 2010, A&A, 522, A19
Wu, Y., Wei, Y., Zhao, M., et al. 2004, A&A, 426, 503
Yang, B., Stancil, P. C., Balakrishnan, N., & Forrey, R. C. 2010, ApJ, 718, 1062
Ybarra, J. E., & Lada, E. A. 2009, ApJ, 695, L120
Young, K. E., Harvey, P. M., Brooke, T. Y., et al. 2005, ApJ, 628, 283